LAWRENCE
LIVERMORE
NATIONAL
LABORATORY

LLNL-TR-838821

M4SF-22LL010302052-Radionuclide Incorporation Model for Corrosion Products

E. Balboni, M. Zavarin, S. Han, K. Smith, K. Booth, L. Moreau, J. Wimpenny, A. B. Kersting

August 16, 2022

Disclaimer

This work performed under the auspices of the U.S. Department of Energy by Lawrence Livermore National Laboratory under Contract DE-AC52-07NA27344.

July 15, 2022

M4SF-22LL010302052-Radionuclide Incorporation Model for Corrosion Products

E. Balboni[1], M. Zavarin[1], S. Han[1], K. Smith[2], C. Booth[2], L.M. Moreau[2], J. Wimpenny[1], A.B. Kersting[1]

[1] Glenn T. Seaborg Institute, Physical & Life Sciences, Lawrence Livermore National Laboratory, 7000 East Avenue, Livermore, CA 94550 USA.
[2] Lawrence Berkeley National Laboratory, One Cyclotron Road, Mailstop 70A1150, Berkeley, CA 94720 USA

DISCLAIMER

Contents

1. Introduction

This progress report (Level 4 Milestone Number M4SF-22LL010302052) summarizes research conducted at Lawrence Livermore National Laboratory (LLNL) within the Crystalline Activity Number SF-22LL01030205. The research is focused on actinide and radionuclide sequestration in steel corrosion products.

Fuel matrix degradation models suggest that the near field is likely to be reducing at the time of canister breaching, steel corrosion, and radionuclide release, but more oxidizing conditions may prevail in the far field. The incorporation of radionuclides into corrosion phases may limit the rate of radionuclide release by sequestering a portion of the radionuclide source term. For these reasons there is a need to evaluate the incorporation of Pu and other radionuclides into various Fe-oxide phases, and to understand the behavior of coprecipitated phases during mineral recrystallization processes and during re-oxidation events. Radionuclide coprecipitation with Fe minerals may impact long-term repository performance and is an ongoing research focus at Lawrence Livermore National Laboratory.

Our FY22 effort focused on completing our analysis of radionuclide incorporation into Fe oxide phases and evaluation of λ_{Me} values across a range of radionuclides relevant to performance assessment models. A draft manuscript summarizing the methodology was prepared using selenium sorption/coprecipitation into iron oxide phases as a test case. Based on our assessment of the relevance of this process in radionuclide retention and sequestration in corrosion products, we plan to initiate focused corrosion and coprecipitation experiments in late FY22/23 that will address the limitations of data available in the literature. For example, no data are available for the incorporation of I into corrosion products. As a result, we are not able to assess its potential impact on I migration from repository near fields.

We are also preparing a draft manuscript on the surface complexation modeling of Se on iron oxide mineral phases using our L-SCIE database and new workflows that comprehensively optimize reaction stoichiometries that have been previously suggested in the literature. These analyses will be linked to our analysis of Se incorporation into iron oxides in FY23.

2. Plutonium coprecipitation with calcite

Balboni, E., Smith, K.F., Moreau, L.M, Wimpenny, J., Booth, C.H., Kersting, A.B., and Zavarin, M. 2021. Plutonium coprecipitation with calcite, ACS Earth and Space Chemistry, 5: 3362-3374. https://doi.org/10.1021/acsearthspacechem.1c00181

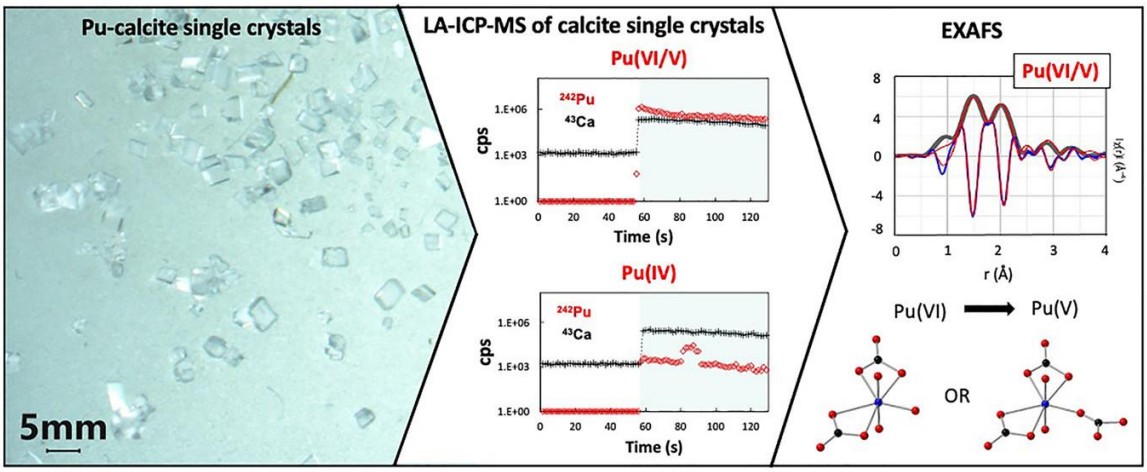

Figure 1. Left panel: mm-sized calcite crystals were synthesis from aqueous solution with Pu(VI) or Pu(IV); central panel: calcite crystals were prepared for laser ablation inductively coupled plasma mass spectrometry to determine the extent of Pu incorporation within individual crystals; right panel: powdered calcite samples were prepared for EXAFS/XANES measurements to determine Pu coordination and oxidation state.

The following is a short summary of a FY22 publication describing the incorporation of plutonium into calcite (Balboni et al., 2021). The mobility of plutonium (Pu) in the subsurface is affected by Pu-mineral interactions such as adsorption-desorption and structural incorporation. Calcite ($CaCO_3$) is a common secondary phase in near surface environments and a major component of many rocks and soils. In geological repositories, calcite is expected to form as an alteration product of cement-based materials. The reactivity of the calcite surface and its ability to tolerate significant variations in its chemical composition through substitution of Ca for other cations make calcite a potentially important sink for environmental contaminants. Here, single crystals of calcite were synthesized from aqueous solutions containing Pu either as Pu(VI) or Pu(IV) and characterized using a combination of laser ablation inductively coupled plasma mass spectrometry (LA-ICP-MS) and x-ray absorption spectroscopy (XAS). These data are used to assess the amount, structure, and oxidation state of Pu coprecipitated into calcite, providing insight into the potential for Pu sequestration in calcite precipitates. Overall, the XAS and LA-ICP-MS data support the coprecipitation of plutonyl in the bulk calcite, though the exact nature of the complex is difficult to elucidate. The coprecipitated plutonyl could be either incorporated in distorted Ca lattice sites or in defect sites. We provide evidence to suggest that Pu(VI) is reduced to Pu(V) during calcite synthesis, but no further reduction to Pu(IV) is observed. The LA-ICP-MS additionally shows that the coprecipitation of Pu(VI/V) is favored over the coprecipitation of Pu(IV). Overall, our results suggest that Pu sequestration in calcite under environmental conditions could immobilize Pu and isolate it from groundwater interactions in contaminated environments

and nuclear waste repositories. This work is follows a similar analysis of Pu incorporation into iron oxide phases (Balboni et al., 2020).

3. Selenium (Se) interaction with iron oxide minerals: a comprehensive analysis of sorption and coprecipitation data across Se oxidation states spanning -II to VI.

3.1 Selenium

Se occurs in high-level nuclear waste (HLW) in the form of radionuclide ^{79}Se, which plays an important role in long-term safety assessments of deep geological repositories (Jörg et al., 2010). ^{79}Se is a pure beta-emitting nuclide, which poses a challenging task for reliable, quantitative determination of its half-life due to vulnerable radiometric and mass spectrometric methodologies, both requiring chemical purification in advance for the removal of interfering activity and isobars. The most recent measurements of ^{79}Se half-life report a value of $3.27(8)\times10^{5}$ (Jörg et al., 2010). Due to its long half-life, it is one of only a few nuclides that determine the long-term radiological impact and of a repository on the environment (Barescut et al., 2005; Olyslaegers et al., 2005).

In nature Se can occur in five different oxidation states (-II, -I, 0, IV, VI). Se species of the oxidation states Se(-II), Se(-I) and Se(0) are characterized by forming sparingly soluble compounds, including metal selenides or elemental Se (Séby et al., 2001). By contrast the two higher oxidations states, where Se forms the oxyanions selenite [$Se^{IV}O_3^{2-}$] and selenate [$Se^{VI}O_4^{2-}$] form soluble species, which are generally highly mobile due to their limited interaction with geological materials (Fernández-Martínez and Charlet, 2009; Grambow, 2008; Séby et al., 2001). In soils in contact with the atmosphere for example, the thermodynamically favored Se species are the oxyanions selenate [Se(VI)] and selenite [Se(IV)]. The oxidation state is therefore the key factor determining the biogeochemical behavior of Se, since parameters such as solubility, mobility, bioavailability and toxicity mainly depend on the occurrence of dissolved Se species (Nothstein et al., 2016; Winkel et al., 2015).

The Se oxidation state in HLW and the accompanying dominant Se species depends on the waste type. Recent research has demonstrated that ^{79}Se occurs as Se(−II) in spent nuclear fuel (Curti et al., 2015; Curti et al., 2014). Due to the reducing conditions predicted in deep repositories, formation of mobile Se species is unlikely, however, it cannot be fully excluded that oxidation processes induced by long-term irradiation could lead to a transformation to Se(VI) (Bingham et al., 2011). The fate of Se in the near-field of high-level radioactive waste also depends on the Se valence state in vitrified glasses which are part of the technical barrier in the multibarrier concept for HLW disposal (Grambow, 2008). The expected predominant Se oxidation state in vitrified HLW arising from nuclear fuel reprocessing plants is Se(IV) in the form of selenite (Bingham et al., 2011).

For the reasons discussed above, to determine long-term safety and performance of nuclear repository it is imperative to understand the mobility of oxidized and reduced forms of Se in oxidizing and reducing conditions.

3.2 Sorption processes: adsorption, surface mediated reduction and coprecipitation

3.2.1 Adsorption studies

The fate of dissolved Se(IV) and Se(VI) species in subsurface systems is primarily determined by interaction with mineral phases, including processes such as adsorption, incorporation, and reductive precipitation, which are the key immobilization mechanisms (Chen et al., 1999; Grambow, 2008). However, most natural materials like clays or silicate minerals show only a restricted retention capacity for Se oxyanions (Missana et al., 2009a). In this context, crystalline iron (oxyhydr)oxide minerals (e.g. hematite and goethite) and their metastable precursors (e.g. ferrihydrite) are of great importance as they are widespread in nature and capable of anion sorption (Adegoke et al., 2013; Roh et al., 2000). This is the reason why, in particular, the mechanisms of Se oxyanion adsorption to iron oxide surfaces have been investigated in detail by a large number of previous studies.

Adsorption of Se(IV) and Se(VI) onto iron oxides can be very efficient at lower pH but is limited under near-neutral and alkaline pH conditions (Balistrieri and Chao, 1990b; Duc et al., 2003; Martínez et al., 2006; Rovira et al., 2008; Zhang and Sparks, 1990). This tendency is independent of the type of iron oxide, since alkaline conditions generally lead to the formation of a negative charge at the iron oxide surface and therefore to a poor adsorption of anionic species (Fernández-Martínez and Charlet, 2009). Moreover, all iron oxides show a relatively high adsorption capacity for Se(IV) and there is only little release of Se(IV) with increasing ionic strength. Unlike Se(IV), adsorption of Se(VI) is much lower and is strongly influenced by the presence of competing anions (Hayes et al., 1987; Jordan et al., 2014b; Jordan et al., 2013; Rietra et al., 2001; Su and Suarez, 2000). Most authors suggest the difference between Se(IV) and Se(VI) adsorption is due to the nature of the chemical attachment and the formation of different types of adsorption complexes. Selected published Kd values for Se(-II), Se(V) and Se(VI) are reported in Table 1.

Table 1. Selected sorption K_d of Se onto geologic materials

Study	Se	Geologic material	Kd (as reported)
Borsig et al. (2018)	Se(VI)	magnetite (pH=9-9.3)	2.14-4.72 log K_d (L/kg)
	Se(IV)	magnetite (pH=9-9.3)	4.7-5.16 log K_d (L/kg)
Missana et al. (2009a)	Se(IV)	smectite (pH 5-6)	200 mL/g
		illite (pH 5-6)	110 mL/g
Loyo et al. (2008)	Se(IV)	magnetite (pH 5)	3500-3600 mL/g
		magnetite (pH 10)	170 mL/g
		Fe/Fe_3C (pH 5)	3640-3800 mL/g
		Fe/Fe_3C (pH 10)	388-410 mL/g
Kim et al. (2012)	Se(IV)	magnetite (pH 7)	2000 mL/g
		magnetite pH 7 (10mmol/L carbonate-)	1300 mL/g
		magnetite (pH 9)	1200 mL/g
		magnetite (pH 9)	300 mL/g
	Se(VI)	magnetite a(6-8) (10mmol/L carbonate-)	no sorption
Fevrier et al. (2007)	Se(IV)	soil (sterile)	16 L/kg
		soil (non-sterile)	130 L/kg
Iida et al. (2011)	Se(-II)	granodiorite (pH 8.5-11.5)	2.2×10^{-4} to 4.0×10^{-3} m^3/kg
	Se(-II)	sandy mudstone (pH 8.5-11.5)	3.3×10^{-2} to 5.6×10^{-2} m^3/kg
	Se(-II)	tuffaceous sandstone (pH 8.5-11.5)	2.9×10^{-2} to 8.2×10^{-2} m^3/kg

3.2.2 Coprecipitation studies

The coprecipitation and structural incorporation of a metal species in a mineral host can be relevant in cases where mineral phases interact with dissolved species during their formation or transformation, including recrystallization or sorption induced crystal growth. Since the formation pathway of crystalline iron oxides commonly includes amorphous metastable intermediates (Schwertmann and Cornell, 2000), such processes are very common in natural systems like soils. Oxyanion incorporation or occlusion by Fe(II) and Fe(II/III) minerals has been shown for Si(IV) (Liu et al., 2012), P(V) (Galvez et al., 1999), As(V) (Bolanz et al., 2013; Das et al., 2015), and Tc(VII) (Skomurski et al., 2010). For this reason, it is conceivable that a retention mechanism on the basis of incorporation also exists for both Se oxyanions, Se(IV) and Se(VI), and that such mechanisms could affect the migration of dissolved Se species.

In reducing conditions, where reduced Se species are more stable, pyrite (FeS_2) and mackinawite (FeS) are expected to be the most dominant Fe(II) minerals. Pyrite is the most common near-surface iron sulfide, well-known for its capacity to incorporate elements up to several mol% (Abraitis et al., 2004; Morse, 1994; Morse and Luther,

1999; Rickard and Luther, 2007). Pyrite is also part of host rocks and bentonite backfill considered for use in HLW repositories (Bildstein et al., 2006; De Craen et al., 2004; Gaucher et al., 2004; Joseph et al., 2011) and could form from the corrosion of steel containers containing vitrified nuclear waste. Due to the similarities in geochemical behavior and ionic radii of Se(-II) and S(-II), iron sulfide minerals are likely host for selenide incorporation. A summary of the coprecipitation studies results is reported in Table 2. Although there is a significant body of literature discussing sorption processes of Se species with various reduced Fe minerals (Fe(II) and mixed Fe(II/FeIII)), there is a lack of information regarding the fate of Se species during re-oxidation. Future studies should focus on determining the retention mechanisms of Se species after extended exposure to oxidative conditions, as has been done for Tc.

Table 2 Summary of Se coprecipitation studies with Fe minerals (n.d.= not determined in study)

Study	**Mineral**	**Se form**	**Se uptake (%)**	**Se behavior upon coprecipitation**
Borsig et al. (2018)	Magnetite (pH 9.2)	Se(IV)	100%	Reduction of Se(IV) or Se(VI) to Se(−II) causes the formation of nanoparticulate iron selenide [FeSe] phase. Progressive oxidation of iron(II) hydroxide and GR into magnetite leads to oxidation of Se(−II) to Se(0) (gray elemental Se)
		Se(VI)	100% (10^{-4}-10^{-3} mol/L); 30% 10^{-2} mol/L	
Diener and Neumann (2011)	Pyrite, mackinawite (pH 4.5-5)	Se(-II)	98.9% (pyrite); 95.4% (mackinawite); 99.2% (amorphous FeS); 98.1% (mixed iron sulfide phases	Focused ion beam analysis shows an inhomogeneous Se distribution with a higher accumulation in the center of the pyrite grains, probably due to the progressive depletion of Se from solution with regard to S.
Diener et al. (2012)	Pyrite, mackinawite (pH 3.7-5)	Se(-II) Se(IV)	98.6 - 99.98 %	In supersaturated solutions: substitution of S(-I) by Se(-I) in Se-doped pyrite and of S(-II) by Se(-II) in Se-doted mackinawite. At lower concentrations and in case of a slower precipitation : Se(-II) and Se(IV) retention by incorporation is coupled with a change in the oxidation state and Se is incorporated as Se(0) into pyrite without structural bonding.
Francisco et al. (2018)	Ferrihydrite (pH 5-10)	Se(IV)	94-99% During aging, the behavior of Se(IV) varied with pH. At pH 5, Se was retained in the solid. At pH 10, a fraction of Se(IV) was released in solution.	Se(IV) was retained within the crystalline post-aging products and possibly occluded in nanopore and defect structures.
Borsig et al. (2017)	Ferrihydrite to hematite (pH 7.5)	Se(IV)	100%	Se oxidation state is not changed during adsorption or coprecipitation. Se coprecipitation leads to the occurrence of a resistant, non-desorbable Se fraction. Se initially adsorbs to the ferrihydrite surface, but after the transformation of ferrihydrite into hematite, it is mostly incorporated by hematite.
		Se(VI)	15%	

Collectively, these sorption studies indicate that sorption processes of Se with Fe(III)(oxy)hydroxide, Fe(II) sulfide, and Fe(II/III) minerals provide a good medium of immobilization for Se. Key factors that affect removal of Se from solution include mineral formation pathways, presence of Fe(II), pH and redox potential, and presence of competing anions.

Regarding the behavior of Se in the geosphere, reductive Se precipitation represents an efficient mechanism to immobilize dissolved Se oxyanions. Processes like these should be considered in safety assessments of HLW disposal sites, as they may affect the migration of the radionuclide ^{79}Se as it interacts with secondary iron oxides in the near-field.

Using data available in the literature regarding Se adsorption and coprecipitation processes, we calculated λ_{Me} values across a range of radionuclides relevant to performance assessment models. Details of the calculations are reported below.

3.3 A semiquantitative approach to radionuclide sorption and coprecipitation processes

The processes of sorption and coprecipitation of a trace element within a mineral matrix can be parameterized using the Doerner-Hoskins (1925) relationship. It is based on the relationship between the trace metal and major element in solution and on the surface of a precipitating phase such that:

$$\lambda_{Me} = \frac{X_{Me}}{X_{Fe}} \times \frac{[Fe]}{[Me]} \quad (1)$$

where X refers to the mol fraction of the trace metal or major element on the surface and the [Fe] and [Me] refer to the aqueous concentration of the trace metal and major element in solution. In this work, Fe oxide minerals are the only mineral phase considered, thus Fe is the major element.

For a closed system coprecipitation experiment, the logarithmic law can be used to determine λ from the initial and final concentrations of the major and trace element during a coprecipitation reaction such that:

$$ln\left(\frac{[Me]}{[Me]_0}\right) = \lambda_{Me} ln\left(\frac{[Fe]}{[Fe]_0}\right) \quad (2)$$

where $[Me]_0$ and $[Fe]_0$ refer to the initial aqueous concentration of the trace metal and major element, respectively and [Me] and [Fe] are the aqueous concentration of the trace metal and major element during the coprecipitation experiment.

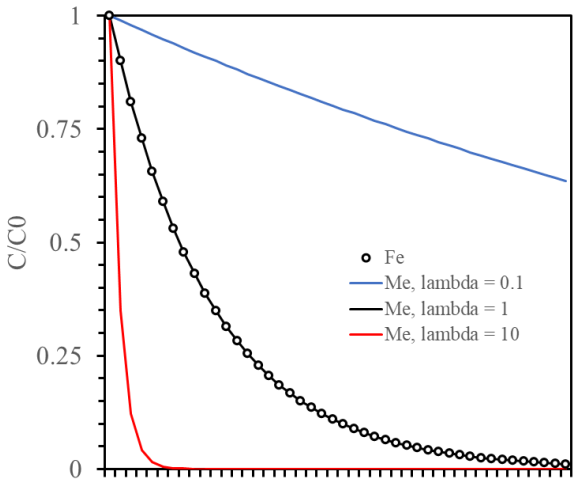

Figure 2. Concentration of trace metal and Fe during precipitation at three different values of lambda based on Equation 2.

The λ values in equations 1 and 2 are defined by Curti (1999) as phenomenological in that the relationship is based on the total concentration of major element and trace metal. The relationship does not account for effects such as pH, ionic strength, fluid composition that may affect the partitioning of the trace metal into the precipitate. Equivalent thermodynamic equations can be written which account for the activity of individual species that participate in the adsorption or coprecipitation process. However, the phenomenological approach is more often reported in the literature.

Equation 1 represents a surface phenomenon that is related to the surface adsorption process that is commonly measured with a Kd parameter. The Kd parameter refers to the concentration of sorbent on a mineral surface relative to its concentration in the aqueous phase:

$$Kd_{Me}(mL/g) = \frac{Me(\frac{mol}{g})}{Me(\frac{mol}{mL})} \quad (3)$$

We can relate adsorption phenomena (often reported as Kd) with coprecipitation phenomena (reported using the Doerner-Hoskins relationship) by converting the Kd value to a λ_{Me} value:

$$\lambda_{Me} = \frac{X_{Me}}{X_{Fe}} \times \frac{[Fe]}{[Me]} = \frac{Me(\frac{mol}{g})}{Fe(\frac{mol}{g})} \times \frac{[Fe]}{\left[\frac{Me(\frac{mol}{g})\times 1000}{Kd_{Me}(\frac{mL}{g})}\right]} = \frac{[Fe]}{Fe(\frac{mol}{g})} \times \frac{Kd_{Me}}{1000} \quad (4)$$

where Fe(mol/g) refers to the concentration of surface Fe atoms per gram of solid phase. Assuming that the trace metal concentration is low, the concentration of Fe atoms is equivalent to the reactive site concentration on the surface. Thus, equation 4 can be further simplified to:

$$\lambda_{Me} = \frac{[Fe]}{\left(\frac{SA\times 10^{18}\times\sigma}{NA}\right)} \times \frac{Kd_{Me}\left(\frac{mL}{g}\right)}{1000} = \frac{602.2\times[Fe]\times Kd_{Me}}{SA\times\sigma} \quad (5)$$

where SA is the surface area of the mineral (m^2/g) and σ is the reactive site density on the surface (sites/nm^2). Equation 5 now allows us to determine λ based on reported sorption Kd values. The λ value calculated for adsorption experiments can then be directly compared to λ values from coprecipitation experiments. In the following paragraph we provide example on how these equations can be used to compare sorption and coprecipitation data for Se and other radionuclides, when data are available.

3.4 Sorption reactions and λMe

To evaluate Se sorption to iron oxides, we take advantage of the community data available in the L-SCIE (Zavarin et al., 2022) database. Below, we provide a summary of the sorption data by plotting surface area normalized Kd (L/kg) values (Ka, L/m^2) for all Se-iron oxide sorption data included in the L-SCIE database. While this is only the first step is developing a λ_{Me} value that can be compared with coprecipitation λ_{Me} values, we are continuing to pursue numerical approaches that can merge the two observed Se sequestration processes (i.e. adsorption and coprecipitation).

When comparing community datasets, the data yield significant variability (e.g. Figure 3). It is important to account for the uncertainty associated with the reported values as well as other processes that may lead to differences in the apparent surface area normalized Ka values (e.g. site saturation effects, solution conditions, etc.). However, a qualitative analysis may be performed by comparing the yield weighted average surface area normalized Ka value. When comparing the behavior of Se(IV) and Se(VI) sorption to hydrous ferric oxide between pH 5 and 9, the difference in log(Ka), $\log(Ka)_{Se(IV)} - \log(Ka)_{Se(VI)}$, is 1.8. Importantly, the difference in λ_{Me} value for Se coprecipitation in Fe(III)oxides described in Section 3.5 yields a nearly equivalent relationship between the coprecipitation $\log(\lambda_{Me})$ for Se(IV) and Se(VI): $\log(\lambda_{Se(IV)}) - \log(\lambda_{Se(VI)}) = 1.9$. Thus, it appears that a relationship between Se sorption and coprecipitation can be established using the λ_{Me} formalism.

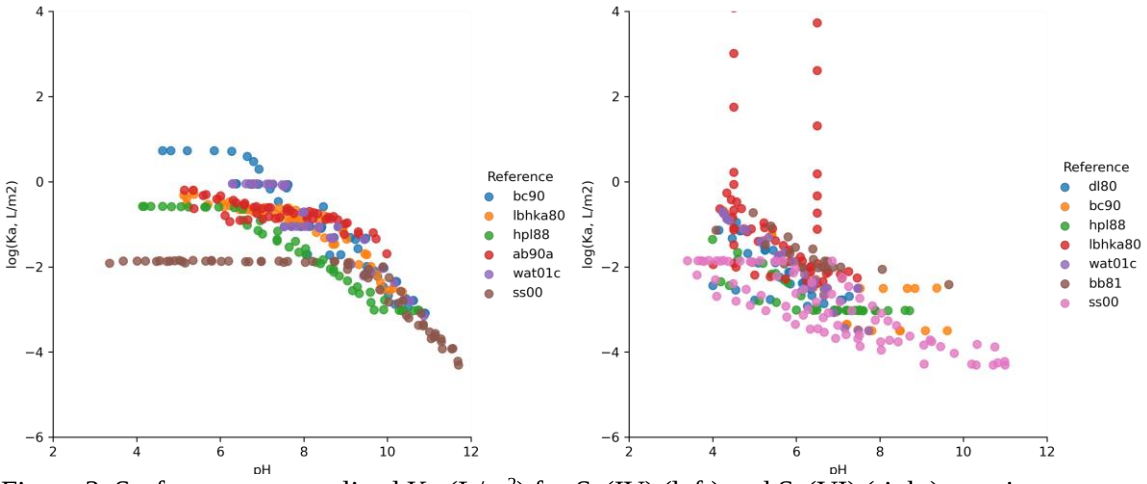

Figure 3. Surface area normalized Ka (L/m^2) for Se(IV) (left) and Se(VI) (right) sorption to hydrous ferric oxide. Bc90 = (Balistrieri and Chao, 1990a); lbhka80 = (Leckie et al., 1980); hpl88 = (Hayes et al., 1988); ab90a = (Anderson and Benjamin, 1990); wat01c = (Wang et al., 2001b); ss00 = (De Craen et al., 2004); dl80 = (Davis and Leckie, 1980); bb81 = (Benjamin and Bloom, 1981).

A similar comparison between Se(IV) and Se(VI) sorption to goethite can be performed. Again, variability among community datasets appears to be quite large (Figure 4). However, the yield weighted relationship clearly shows a preference of Se(IV) over Se(VI) for the goethite surface. When comparing the behavior of Se(IV) and Se(VI) sorption to goethite between pH 5 and 9, the difference in log(Ka), $\log(Ka)_{Se(IV)} - \log(Ka)_{Se(VI)}$, is 1.9 and consistent with the relationship found in coprecipitation experiments (1.9).

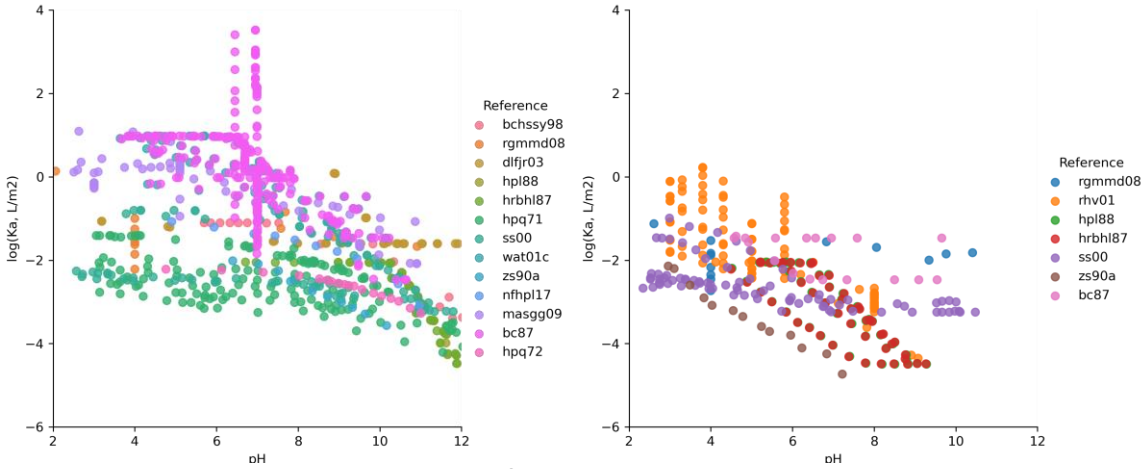

Figure 4. Surface area normalized Ka (L/m^2) for Se(IV) (left) and Se(VI) (right) sorption to goethite. Bchssy98 = (Boult et al., 1998); rgmmd08 = (Rovira et al., 2008); dlfjr03 = (Duc et al., 2003); hpl88 = (Hayes et al., 1988); hrbhl87 = (Hayes Kim et al., 1987); hpq71 = (Hingston et al., 1971); ss00 = (De Craen et al., 2004); wat01c = (Wang et al., 2001b); zs90a =(Zhang and Sparks, 1990); nfhpl17 = (Nie et al., 2017); masgg09 = (Missana et al., 2009b); bc87 = (Balistrieri and Chao, 1987); hpq72 = (Kingston et al., 1972); rhv01 = (Rietra et al., 2001).

A similar comparison between Se(IV) and Se(VI) sorption to hematite can be performed. However, the number of data available are more limited (Figure 5). Nevertheless, the yield weighted relationship still shows a preference of Se(IV) over Se(VI) for the goethite surface. When comparing the behavior of Se(IV) and Se(VI) sorption to goethite between pH 5 and 9, the difference in log(Ka), $\log(Ka)_{Se(IV)} - \log(Ka)_{Se(VI)}$, is 0.3. This value is particularly low likely as a result of the low surface area and nearly undetectable sorption observed in most experiments. We hypothesize that the difference in Se(IV) and Se(VI) behavior would likely be comparable to goethite and hydrous ferric oxide if higher concentrations of hematite and/or higher surface area hematite were used in batch sorption experiments.

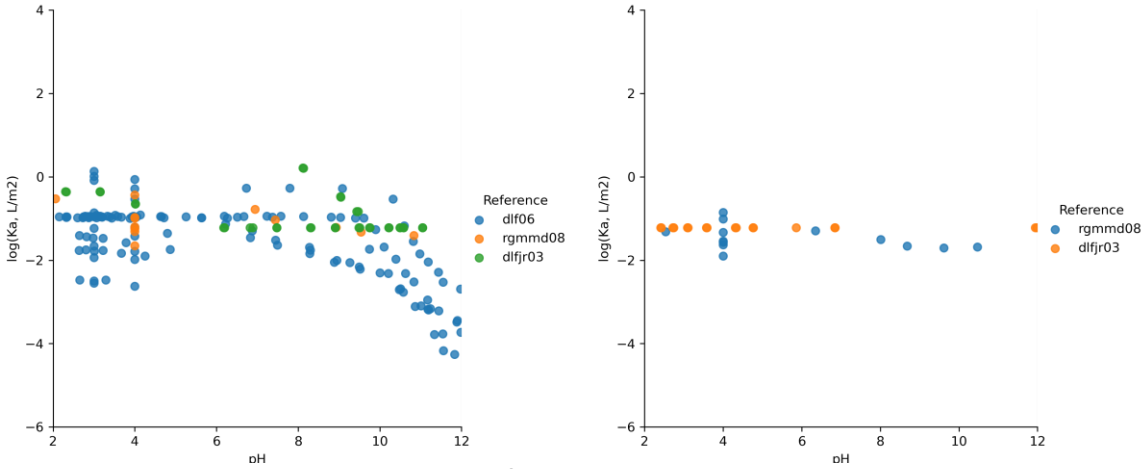

Figure 5. Surface area normalized Ka (L/m^2) for Se(IV) (left) and Se(VI) (right) sorption to hematite. Dlf06 = (Duc et al., 2006); rgmmd08 = (Rovira et al., 2008); dlfjr03 = (Duc et al., 2003).

A comparison between Se(IV) and Se(VI) sorption to maghemite can be performed and yield a somewhat different relationship between the two Se oxidation states. The number of data available are also limited (Figure 6). Nevertheless, the yield weighted relationship still shows a preference of Se(IV) over Se(VI) for the maghemite surface. When comparing the behavior of Se(IV) and Se(VI) sorption to goethite between pH 5 and 9, the difference in log(Ka), $\log(Ka)_{Se(IV)} - \log(Ka)_{Se(VI)}$, is 0.8. This value may be low as a result of the limited available data. Alternatively, the difference in Se(IV) and Se(VI) behavior may also be lower than that of goethite and hydrous ferric oxide due to the likely presence of Fe(II) in the system and potential reduction of Se(VI) to Se(IV) during the experiments. Importantly, the difference in λ_{Me} value for Se coprecipitation in Fe(II)/(III)oxides described in Section 3.5 yields a nearly equivalent relationship between the coprecipitation $\log(\lambda_{Me})$ for Se(IV) and Se(VI): $\log(\lambda_{Se(IV)}) - \log(\lambda_{Se(VI)}) = 0.7$. Thus, we can conclude that the relationship between sorption and coprecipitation data for Fe(II)/Fe(III) oxides is valid and consistent with the relationship observed for hydrous ferric oxide and goethite sorption and coprecipitation data.

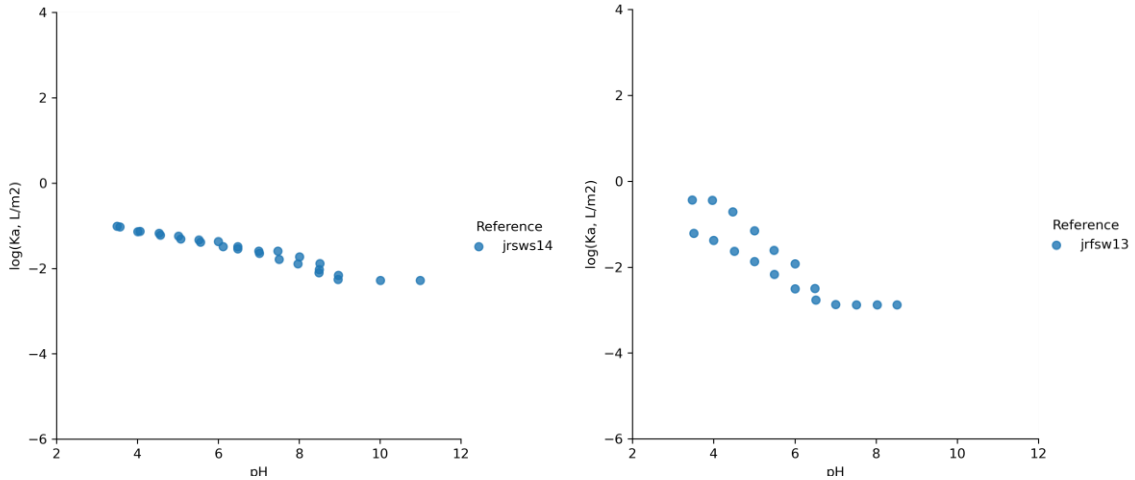

Figure 6. Surface area normalized Ka (L/m^2) for Se(IV) (left) and Se(VI) (right) sorption to maghemite. jrsws14 = (Jordan et al., 2014a); jrfsw13 = (Jordan et al., 2013).

The comparison between Se(IV) and Se(VI) sorption to magnetite was also performed. Again, the number of data available are limited (Figure 7). Nevertheless, the yield weighted relationship still shows a preference of Se(IV) over Se(VI) for the magnetite surface. When comparing the behavior of Se(IV) and Se(VI) sorption to goethite between pH 5 and 9, the difference in log(Ka), $\log(Ka)_{Se(IV)} - \log(Ka)_{Se(VI)}$, is 1.0. This value is similar to that of maghemite and may reflect the presence of Fe(II) and reduction of Se(VI) to Se(IV). The difference in log(Ka), $\log(Ka)_{Se(IV)} - \log(Ka)_{Se(VI)}$, is also consistent with the relationship found in coprecipitation experiments (0.7). The results for all iron oxides show promise for developing a robust relationship between the sorption and coprecipitation of Se to various Fe(III) and mixed Fe(II)/Fe(III) oxide phases and the use of λ_{Me} to account for the sequestration of Se into iron oxide phases through both sorption and coprecipitation.

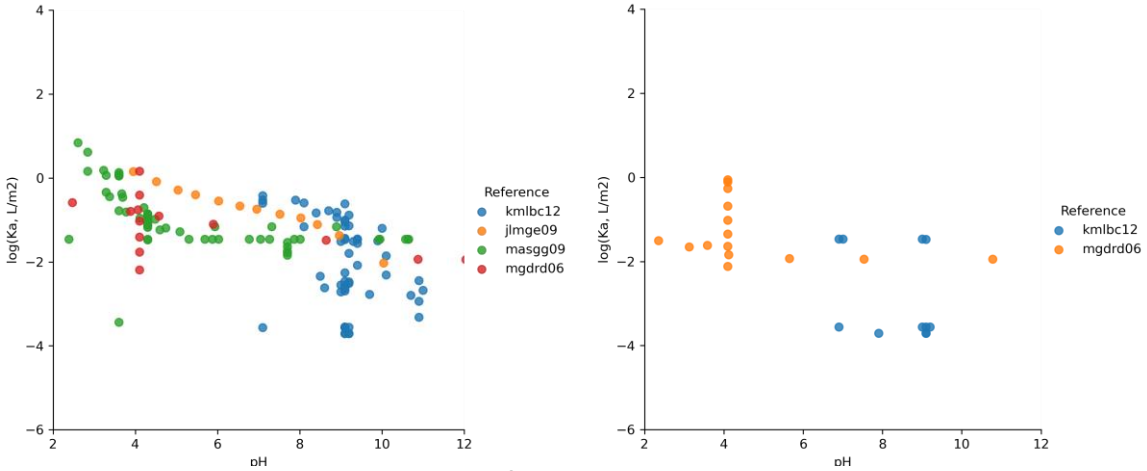

Figure 7. Surface area normalized Ka (L/m^2) for Se(IV) (left) and Se(VI) (right) sorption to magnetite. Kmlbc12 = (Kim et al., 2012); jlmge09 = (Jordan et al., 2009); masgg09 = (Missana et al., 2009b); mgdrd06 = (Martínez et al., 2006).

3.5 Coprecipitation reactions and λMe

We calculated λ_{Me} using equation (2) and data from literature that describe coprecipitation of Tc, Se, Np and Pu in a suite of Fe(II), Fe(II/III) and Fe(III) minerals. Here, we only focus on the Se data. Calculated λ_{Me} values are expected to be high in case of strong contaminant partitioning in mineral phases and low when partitioning of metals is low (Figure 8).

In Figure 8, the values of λ_{Me} (on x axis) are compared to % of radionuclide uptake, which represents how much radionuclide is sequestered by a mineral phase after mineral precipitation. Our results show that overall, the calculated λ_{Me}values increase as the % of coprecipitation increases. For solids that retain <70% radionuclides λ_{Me} is usually <0.1, which is close to what we expected based on Figure 2.

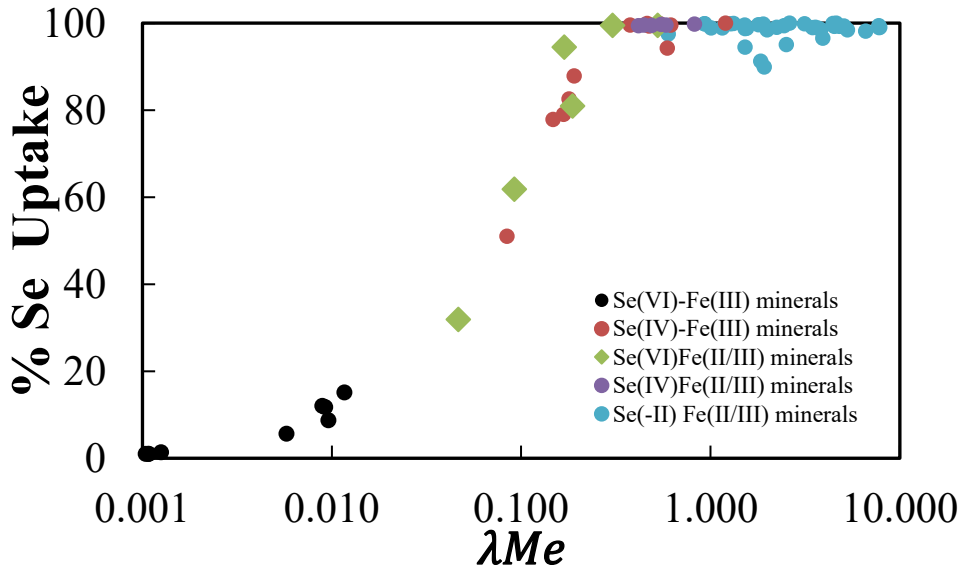

Figure 8. Values of λ_{Me} as a function of Se uptake during coprecipitation reactions

Amongst the radionuclides considered, the Se literature is the most comprehensive in addressing Se coprecipitation behavior with Fe minerals, and the calculated λ_{Me} span the largest range (0.001-8). Borsig et al. (Borsig et al., 2018; Börsig et al., 2017) and Diener et al. (Diener and Neumann, 2011; Diener et al., 2012) provide comprehensive data sets of Se (VI, IV, -II) coprecipitation with various Fe oxide minerals including Fe(III), mixed Fe(II/III) and Fe sulfides and their data sets were analyzed to determine trends in the calculated λ_{Me} values.

The lowest values of λ_{Me} are observed for Se(VI) coprecipitation with Fe(III) minerals (Figure 9). The λ_{Me} values increase slightly for coprecipitation of Se(VI) with reduced Fe minerals and became higher for Se(IV) coprecipitated with mixed Fe(II/III) minerals. The highest λ_{Me} values are measured for reduced selenium (-II) in coprecipitation reaction

with reduced Fe minerals, such as pyrite. This general trend seems to be consistent with Se geochemical behavior observed in sorption reactions.

Although a few assumptions need to be made to calculate λ_{Me} (specifically regarding the [Fe_0] concentration) we conclude that λ_{Me} provides a valid approach to describe radionuclide coprecipitation behavior with Fe minerals from data sourced from the literature.

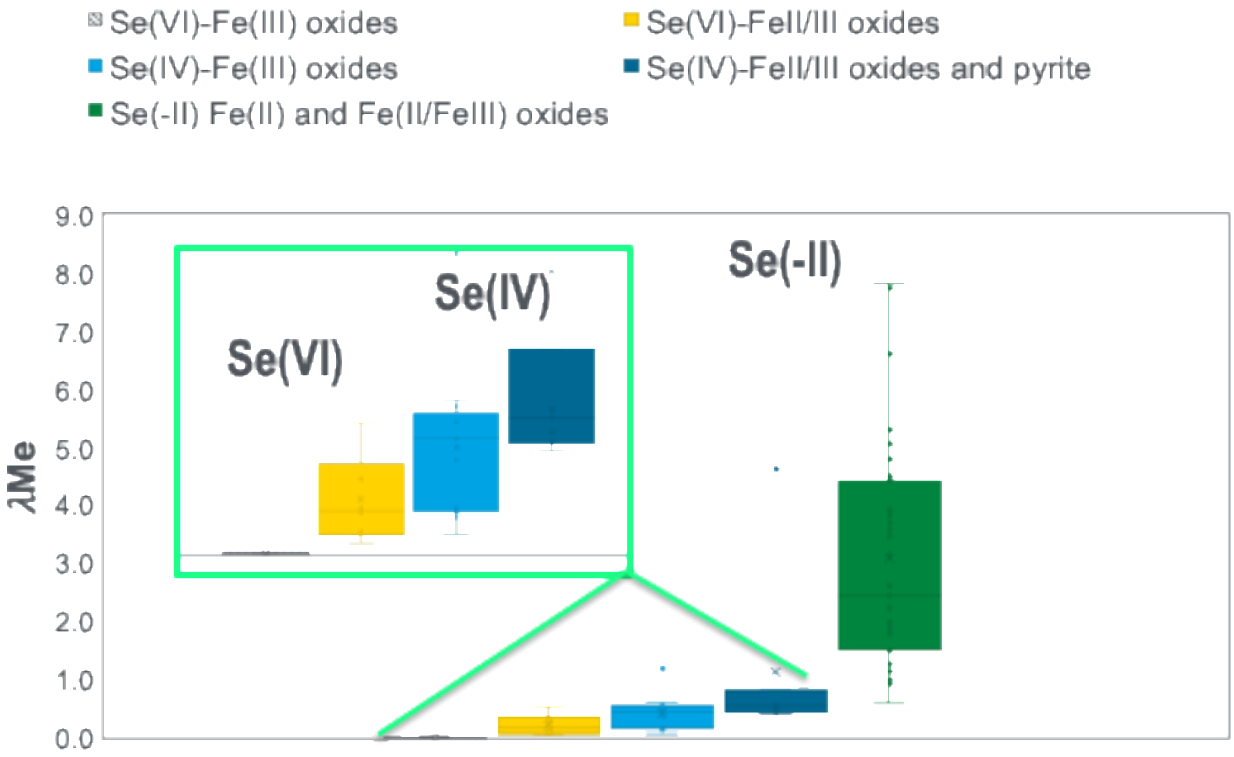

Figure 9. λMe calculated for coprecipitation reactions of Se with Fe minerals

3.8 Future outlook: λMe application

To date, we have examined both the sorption and coprecipitation of various Se oxidation states to a number of iron oxides solid phases. While additional research is needed to determine the numerical representation of these processes, the empirical λ_{Me} values shows promise in unifying the observed sorption and coprecipitation behavior of Se to steel corrosion products. In FY22/23, we plan to complete our analysis of Se behavior and extend this approach to other radionuclides of relevance to the nuclear waste repository performance assessment modeling effort. The coprecipitation data analysis has largely been completed while the extension to sorption data available in the L-SCIE database is ongoing. In FY23, we will extend this approach to complete our assessment of radionuclide interaction with steel corrosion products and its impact on radionuclide release and migration from the nuclear waste repository near field.

4. A comprehensive surface complexation reaction analysis workflow: Surface complexation of Se(IV) and Se(VI) on iron oxide phases

4.1 Development of radionuclide surface complexation modeling framework

Surface complexation models (SCM), which address the quantification of sorption processes, play a key role in Generic Disposal System Assessment (GDSA). Although enormous amounts of efforts have been made to develop reliable SCMs, obtaining global consensus among reported SCMs is still challenging since each SCM had been constructed with different foundations. In light of the limitation, this task aims at developing a more comprehensive SCM framework by compiling raw sorption data and the relevant surface complexation reactions reported from various literature sources. Figure 10 describes the developed framework for SCM database development. The framework consists of sorption database, i.e., L-SCIE (LLNL Surface Complexation/Ion Exchange) (Zavarin et al., 2022), a surface titration model, and a surface complexation model. L-SCIE database provides input data for surface titration/complexation models, and data processing and fitting routine have been done within each model.

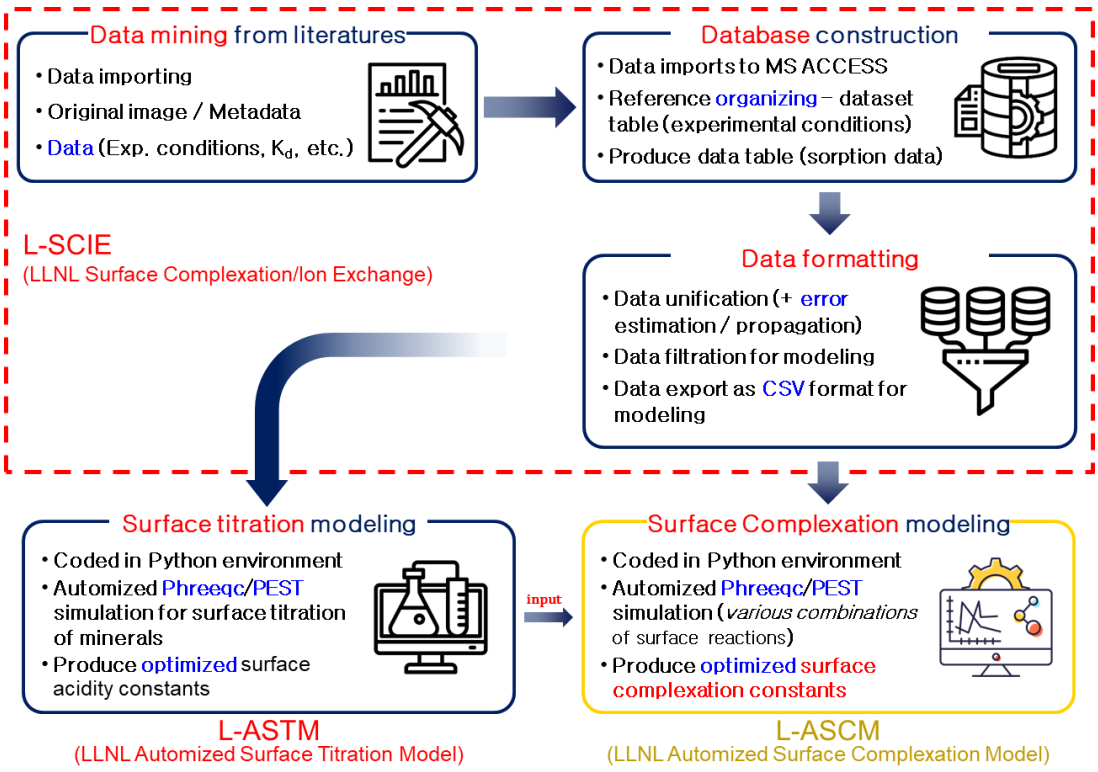

Figure 10. Workflow of radionuclide surface complexation modeling framework.

The newly developed SCM, LLNL Automized Surface Complexation Model (L-ASCM), was written in Python and the model includes three major components: data processing

for input file generation, data fitting routine integrated with PHREEQC (Parkhurst and Appelo, 2013) and PEST (Doherty, 2018), and post-processing part for simulation evaluation (Figure 11). One of the key features of the current model is that the model enables automation of the entire modeling process, for example, pre data analysis, input file generation, execution of data fitting routine, post simulation analysis, and visualization of simulation results. Furthermore, the model automatically examines the fitting for all possible SCM structural configurations (e.g., types of SCM and surface reactions) without any user interference.

The details in modeling sequence of L-ASCM is shown in Figure 11. First, the code analyzes the integrity of the raw data from database. Since most of data in database manually extracted from the literatures, some data points have unrealistic value, for example, aqueous concentration of adsorbate might have a negative value. For those inappropriate data points, the values are modified, and the model runs PHREEQC simulation to correct the charge balance of each solution. As summarized in Table 3, there could be a number of surface complexation reactions for given mineral and adsorbate pair. The L-ASCM makes a list of all possible surface complexation reaction combinations and generates the relevant PHREEQC/PEST input files for all combinations. Then the code runs simulations for all scenarios and evaluates the quality of fit obtained from each SCM construct. Finally, optimized surface complexation reactions and the relevant constants are produced.

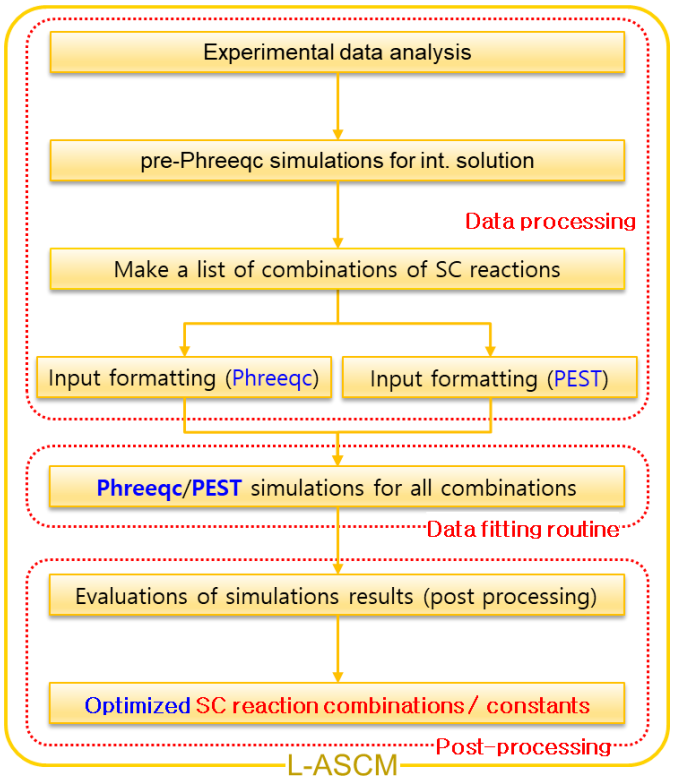

Figure 11. Surface complexation modeling sequence (L-ASCM)

Table 3. Surface complexation reactions of selenium sorption to ferrihydrite as reported in the RES^{3}T database (Brendler et al., 2003; Dresden-Rossendorf, 2013).

	Surface complexation reactions	Initial $\log_{10}K$	Reference
1	$\text{»Fe-OH} + SeO_3^{2-} \leftrightarrow \text{»Fe-OH-}SeO_3^{2-}$	5.17	(Dzombak and Morel, 1990)
2	$\text{»Fe-OH} + SeO_3^{2-} + H^+ \leftrightarrow \text{»Fe-OH}_2\text{-}SeO_3^-$	12.90	(Benjamin and Bloom, 1981)
3	$\text{»Fe-OH} + SeO_3^{2-} + 2H^+ \leftrightarrow \text{»Fe-OH}_2\text{-HSeO}_3$	22.00	(Benjamin and Bloom, 1981)
4	$\text{»Fe-OH} + SeO_3^{2-} + 3H^+ \leftrightarrow \text{»Fe-OH}_2\text{-}SeO_3H_2^+$	29.00[a]	-[*]
5	$2\text{»Fe-OH} + SeO_3^{2-} \leftrightarrow (\text{»Fe-O})_2\text{-}SeO_3^{4-} + 2H^+$	-6.96	(Wang et al., 2001a)
6	$2\text{»Fe-OH} + SeO_3^{2-} + 2H^+ \leftrightarrow (\text{»Fe-OH}_2)_2\text{-}SeO_3$	26.06	(Wang et al., 2001a)

[a]Presumed value. [*]Newly added in this work

4.2 Case study of Se(IV) sorption to ferrihydrite

In this task, a case study of tetravalent selenium sorption to ferrihydrite was conducted to demonstrate the newly developed SCM, L-ASCM. The SCM for the Se(IV)-ferrihydrite system contains 331 datapoints extracted from six publications (Anderson and Benjamin, 1990; Balistrieri and Chao, 1990a; De Craen et al., 2004; Hayes et al., 1988; Leckie et al., 1980; Wang et al., 2001a) and adopted six surface complexation reactions summarized in Table 3. The model employed non electrostatic model (NEM), and the used surface acidity constants (pK_1 and pK_2) of ferrihydrite were 7.29 and 8.93, respectively. Since six surface complexation reactions were used, a total of 63 reaction combinations were obtained (Table 4). In other words, 63 different scenarios had been tested to find appropriate surface complexation reactions which can model the Se(IV) sorption to ferrihydrite. The quality of each model (scenario) was evaluated based on weighted Pearson correlation coefficient (R value), sum of squared weighted residuals (ϕ value), and standard deviation (SD) of surface complexation reaction constant calculated from the model. If the R value is higher than 0.9 and SDs of all reaction constants are lower than 1.0, it was presumed that the model has a good quality.

Table 4 List of surface complexation reaction combinations

Scenario	Surface species	Scenario	Surface species
	One species reaction	**33**	$\text{»Fe-OH}_2\text{-}SeO_3^-$, $\text{»Fe-OH}_2\text{-HSeO}_3$, $(\text{»Fe-O})_2\text{-}SeO_3^{4-}$
1	$\text{»Fe-OH-}SeO_3^{2-}$	**34**	$\text{»Fe-OH}_2\text{-}SeO_3^-$, $\text{»Fe-OH}_2\text{-HSeO}_3$, $(\text{»Fe-OH}_2)_2\text{-SeO}_3$
2	$\text{»Fe-OH}_2\text{-}SeO_3^-$	**35**	$\text{»Fe-OH}_2\text{-}SeO_3^-$, $\text{»Fe-OH}_2\text{-}SeO_3H_2^+$, $(\text{»Fe-O})_2\text{-}SeO_3^{4-}$
3	$\text{»Fe-OH}_2\text{-HSeO}_3$	**36**	$\text{»Fe-OH}_2\text{-}SeO_3^-$, $\text{»Fe-OH}_2\text{-}SeO_3H_2^+$, $(\text{»Fe-OH}_2)_2\text{-SeO}_3$
4	$\text{»Fe-OH}_2\text{-}SeO_3H_2^+$	**37**	$\text{»Fe-OH}_2\text{-}SeO_3^-$, $(\text{»Fe-O})_2\text{-}SeO_3^{4-}$, $(\text{»Fe-OH}_2)_2\text{-SeO}_3$
5	$(\text{»Fe-O})_2\text{-}SeO_3^{4-}$	**38**	$\text{»Fe-OH}_2\text{-HSeO}_3$, $\text{»Fe-OH}_2\text{-}SeO_3H_2^+$, $(\text{»Fe-O})_2\text{-}SeO_3^{4-}$
6	$(\text{»Fe-OH}_2)_2\text{-SeO}_3$	**39**	$\text{»Fe-OH}_2\text{-HSeO}_3$, $\text{»Fe-OH}_2\text{-}SeO_3H_2^+$,

Scenario	Surface species	Scenario	Surface species
			$(»Fe\text{-}OH_2)_2\text{-}SeO_3$
	Two species reaction	**40**	$»Fe\text{-}OH_2\text{-}HSeO_3$, $(»Fe\text{-}O)_2\text{-}SeO_3^{4-}$, $(»Fe\text{-}OH_2)_2\text{-}SeO_3$
7	$»Fe\text{-}OH\text{-}SeO_3^{2-}$, $»Fe\text{-}OH_2\text{-}SeO_3^{-}$	**41**	$»Fe\text{-}OH_2\text{-}SeO_3H_2^{+}$, $(»Fe\text{-}O)_2\text{-}SeO_3^{4-}$, $(»Fe\text{-}OH_2)_2\text{-}SeO_3$
8	$»Fe\text{-}OH\text{-}SeO_3^{2-}$, $»Fe\text{-}OH_2\text{-}HSeO_3$		**Four species reaction**
9	$»Fe\text{-}OH\text{-}SeO_3^{2-}$, $»Fe\text{-}OH_2\text{-}SeO_3H_2^{+}$	**42**	$»Fe\text{-}OH\text{-}SeO_3^{2-}$, $»Fe\text{-}OH_2\text{-}SeO_3^{-}$, $»Fe\text{-}OH_2\text{-}HSeO_3$, $»Fe\text{-}OH_2\text{-}SeO_3H_2^{+}$
10	$»Fe\text{-}OH\text{-}SeO_3^{2-}$, $(»Fe\text{-}O)_2\text{-}SeO_3^{4-}$	**43**	$»Fe\text{-}OH\text{-}SeO_3^{2-}$, $»Fe\text{-}OH_2\text{-}SeO_3^{-}$, $»Fe\text{-}OH_2\text{-}HSeO_3$, $(»Fe\text{-}O)_2\text{-}SeO_3^{4-}$
11	$»Fe\text{-}OH\text{-}SeO_3^{2-}$, $(»Fe\text{-}OH_2)_2\text{-}SeO_3$	**44**	$»Fe\text{-}OH\text{-}SeO_3^{2-}$, $»Fe\text{-}OH_2\text{-}SeO_3^{-}$, $»Fe\text{-}OH_2\text{-}HSeO_3$, $(»Fe\text{-}OH_2)_2\text{-}SeO_3$
12	$»Fe\text{-}OH_2\text{-}SeO_3^{-}$, $»Fe\text{-}OH_2\text{-}HSeO_3$	**45**	$»Fe\text{-}OH\text{-}SeO_3^{2-}$, $»Fe\text{-}OH_2\text{-}SeO_3^{-}$, $»Fe\text{-}OH_2\text{-}SeO_3H_2^{+}$, $(»Fe\text{-}O)_2\text{-}SeO_3^{4-}$
13	$»Fe\text{-}OH_2\text{-}SeO_3^{-}$, $»Fe\text{-}OH_2\text{-}SeO_3H_2^{+}$	**46**	$»Fe\text{-}OH\text{-}SeO_3^{2-}$, $»Fe\text{-}OH_2\text{-}SeO_3^{-}$, $»Fe\text{-}OH_2\text{-}SeO_3H_2^{+}$, $(»Fe\text{-}OH_2)_2\text{-}SeO_3$
14	$»Fe\text{-}OH_2\text{-}SeO_3^{-}$, $(»Fe\text{-}O)_2\text{-}SeO_3^{4-}$	**47**	$»Fe\text{-}OH\text{-}SeO_3^{2-}$, $»Fe\text{-}OH_2\text{-}SeO_3^{-}$, $(»Fe\text{-}O)_2\text{-}SeO_3^{4-}$, $(»Fe\text{-}OH_2)_2\text{-}SeO_3$
15	$»Fe\text{-}OH_2\text{-}SeO_3^{-}$, $(»Fe\text{-}OH_2)_2\text{-}SeO_3$	**48**	$»Fe\text{-}OH\text{-}SeO_3^{2-}$, $»Fe\text{-}OH_2\text{-}HSeO_3$, $»Fe\text{-}OH_2\text{-}SeO_3H_2^{+}$, $(»Fe\text{-}O)_2\text{-}SeO_3^{4-}$
16	$»Fe\text{-}OH_2\text{-}HSeO_3$, $»Fe\text{-}OH_2\text{-}SeO_3H_2^{+}$	**49**	$»Fe\text{-}OH\text{-}SeO_3^{2-}$, $»Fe\text{-}OH_2\text{-}HSeO_3$, $»Fe\text{-}OH_2\text{-}SeO_3H_2^{+}$, $(»Fe\text{-}OH_2)_2\text{-}SeO_3$
17	$»Fe\text{-}OH_2\text{-}HSeO_3$, $(»Fe\text{-}O)_2\text{-}SeO_3^{4-}$	**50**	$»Fe\text{-}OH\text{-}SeO_3^{2-}$, $»Fe\text{-}OH_2\text{-}HSeO_3$, $(»Fe\text{-}O)_2\text{-}SeO_3^{4-}$, $(»Fe\text{-}OH_2)_2\text{-}SeO_3$
18	$»Fe\text{-}OH_2\text{-}HSeO_3$, $(»Fe\text{-}OH_2)_2\text{-}SeO_3$	**51**	$»Fe\text{-}OH\text{-}SeO_3^{2-}$, $»Fe\text{-}OH_2\text{-}SeO_3H_2^{+}$ $(»Fe\text{-}O)_2\text{-}SeO_3^{4-}$, $(»Fe\text{-}OH_2)_2\text{-}SeO_3$
19	$»Fe\text{-}OH_2\text{-}SeO_3H_2^{+}$, $(»Fe\text{-}O)_2\text{-}SeO_3^{4-}$	**52**	$»Fe\text{-}OH_2\text{-}SeO_3^{-}$, $»Fe\text{-}OH_2\text{-}HSeO_3$, $»Fe\text{-}OH_2\text{-}SeO_3H_2^{+}$, $(»Fe\text{-}O)_2\text{-}SeO_3^{4-}$
20	$»Fe\text{-}OH_2\text{-}SeO_3H_2^{+}$, $(»Fe\text{-}OH_2)_2\text{-}SeO_3$	**53**	$»Fe\text{-}OH_2\text{-}SeO_3^{-}$, $»Fe\text{-}OH_2\text{-}HSeO_3$, $»Fe\text{-}OH_2\text{-}SeO_3H_2^{+}$, $(»Fe\text{-}OH_2)_2\text{-}SeO_3$
21	$(»Fe\text{-}O)_2\text{-}SeO_3^{4-}$, $(»Fe\text{-}OH_2)_2\text{-}SeO_3$	**54**	$»Fe\text{-}OH_2\text{-}SeO_3^{-}$, $»Fe\text{-}OH_2\text{-}HSeO_3$, $(»Fe\text{-}O)_2\text{-}SeO_3^{4-}$, $(»Fe\text{-}OH_2)_2\text{-}SeO_3$
	Three species reaction	**55**	$»Fe\text{-}OH_2\text{-}SeO_3^{-}$, $»Fe\text{-}OH_2\text{-}SeO_3H_2^{+}$, $(»Fe\text{-}O)_2\text{-}SeO_3^{4-}$, $(»Fe\text{-}OH_2)_2\text{-}SeO_3$
22	$»Fe\text{-}OH\text{-}SeO_3^{2-}$, $»Fe\text{-}OH_2\text{-}SeO_3^{-}$, $»Fe\text{-}OH_2\text{-}HSeO_3$		$»Fe\text{-}OH_2\text{-}HSeO_3$, $»Fe\text{-}OH_2\text{-}SeO_3H_2^{+}$, $(»Fe\text{-}O)_2\text{-}SeO_3^{4-}$, $(»Fe\text{-}OH_2)_2\text{-}SeO_3$
23	$»Fe\text{-}OH\text{-}SeO_3^{2-}$, $»Fe\text{-}OH_2\text{-}SeO_3^{-}$ $»Fe\text{-}OH_2\text{-}SeO_3H_2^{+}$	**56**	**Five species reaction**
24	$»Fe\text{-}OH\text{-}SeO_3^{2-}$, $»Fe\text{-}OH_2\text{-}SeO_3^{-}$ $(»Fe\text{-}O)_2\text{-}SeO_3^{4-}$	**57**	$»Fe\text{-}OH\text{-}SeO_3^{2-}$, $»Fe\text{-}OH_2\text{-}SeO_3^{-}$, $»Fe\text{-}OH_2\text{-}HSeO_3$, $»Fe\text{-}OH_2\text{-}SeO_3H_2^{+}$, $(»Fe\text{-}O)_2\text{-}SeO_3^{4-}$
25	$»Fe\text{-}OH\text{-}SeO_3^{2-}$, $»Fe\text{-}OH_2\text{-}SeO_3^{-}$, $(»Fe\text{-}OH_2)_2\text{-}SeO_3$	**58**	$»Fe\text{-}OH\text{-}SeO_3^{2-}$, $»Fe\text{-}OH_2\text{-}SeO_3^{-}$, $»Fe\text{-}OH_2\text{-}HSeO_3$, $»Fe\text{-}OH_2\text{-}SeO_3H_2^{+}$, $(»Fe\text{-}OH_2)_2\text{-}SeO_3$
26	$»Fe\text{-}OH\text{-}SeO_3^{2-}$, $»Fe\text{-}OH_2\text{-}HSeO_3$, $»Fe\text{-}OH_2\text{-}SeO_3H_2^{+}$	**59**	$»Fe\text{-}OH\text{-}SeO_3^{2-}$, $»Fe\text{-}OH_2\text{-}SeO_3^{-}$, $»Fe\text{-}OH_2\text{-}HSeO_3$, $(»Fe\text{-}O)_2\text{-}SeO_3^{4-}$, $(»Fe\text{-}OH_2)_2\text{-}SeO_3$
27	$»Fe\text{-}OH\text{-}SeO_3^{2-}$, $»Fe\text{-}OH_2\text{-}HSeO_3$, $(»Fe\text{-}O)_2\text{-}SeO_3^{4-}$	**60**	$»Fe\text{-}OH\text{-}SeO_3^{2-}$, $»Fe\text{-}OH_2\text{-}SeO_3^{-}$, $»Fe\text{-}OH_2\text{-}SeO_3H_2^{+}$, $(»Fe\text{-}O)_2\text{-}SeO_3^{4-}$, $(»Fe\text{-}OH_2)_2\text{-}SeO_3$
28	$»Fe\text{-}OH\text{-}SeO_3^{2-}$, $»Fe\text{-}OH_2\text{-}HSeO_3$, $(»Fe\text{-}OH_2)_2\text{-}SeO_3$	**61**	$»Fe\text{-}OH\text{-}SeO_3^{2-}$, $»Fe\text{-}OH_2\text{-}HSeO_3$, $»Fe\text{-}OH_2\text{-}SeO_3H_2^{+}$, $(»Fe\text{-}O)_2\text{-}SeO_3^{4-}$, $(»Fe\text{-}OH_2)_2\text{-}SeO_3$
29	$»Fe\text{-}OH\text{-}SeO_3^{2-}$, $»Fe\text{-}OH_2\text{-}SeO_3H_2^{+}$,	**62**	$»Fe\text{-}OH_2\text{-}SeO_3^{-}$, $»Fe\text{-}OH_2\text{-}HSeO_3$,

Scenario	Surface species	Scenario	Surface species
	$(\text{»Fe-O})_2\text{-SeO}_3^{4-}$		$\text{»Fe-OH}_2\text{-SeO}_3\text{H}_2^+$, $(\text{»Fe-O})_2\text{-SeO}_3^{4-}$, $(\text{»Fe-OH}_2)_2\text{-SeO}_3$
30	»Fe-OH-SeO_3^{2-}, $\text{»Fe-OH}_2\text{-SeO}_3\text{H}_2^+$, $(\text{»Fe-OH}_2)_2\text{-SeO}_3$		**Six species reaction**
31	»Fe-OH-SeO_3^{2-}, $(\text{»Fe-O})_2\text{-SeO}_3^{4-}$, $(\text{»Fe-OH}_2)_2\text{-SeO}_3$	**63**	»Fe-OH-SeO_3^{2-}, $\text{»Fe-OH}_2\text{-SeO}_3^-$, $\text{»Fe-OH}_2\text{-HSeO}_3$, $\text{»Fe-OH}_2\text{-SeO}_3\text{H}_2^+$, $(\text{»Fe-O})_2\text{-SeO}_3^{4-}$, $(\text{»Fe-OH}_2)_2\text{-SeO}_3$
32	$\text{»Fe-OH}_2\text{-SeO}_3^-$, $\text{»Fe-OH}_2\text{-HSeO}_3$, $\text{»Fe-OH}_2\text{-SeO}_3\text{H}_2^+$		

The simulations results showed that only six combinations, out of 63, can effectively simulate the Se(IV) sorption data (Table 5). Good quality model had not been obtained when one, four, five, and six surface complexation reactions were used. In addition, the contribution of surface species to model quality was observed: »Fe-OH-SeO_3^{2-} species always included in the good quality models, on the other hand, the models never had $(\text{»Fe-O})_2\text{-SeO}_3^{4-}$ species. The best quality model was attained for three surface species model, however, all good quality models had similar R values and ϕ values. Figure 12 describes simulation results obtained from the scenario 22. As shown in the graphs, newly developed SCM can reasonably capture sorption experiment results.

Table 5. Surface complexation models with good quality fit

Number of reactions	Surface species	R value	ϕ value
2	»Fe-OH-SeO_3^{2-}, $\text{»Fe-OH}_2\text{-HSeO}_3$	0.9177	2339
2	»Fe-OH-SeO_3^{2-}, $\text{»Fe-OH}_2\text{-SeO}_3\text{H}_2^+$	0.9110	2629
3	*»Fe-OH-SeO_3^{2-}, $\text{»Fe-OH}_2\text{-SeO}_3^-$, $\text{»Fe-OH}_2\text{-HSeO}_3$*	*0.9232*	*2220*
3	»Fe-OH-SeO_3^{2-}, $\text{»Fe-OH}_2\text{-SeO}_3^-$, $\text{»Fe-OH}_2\text{-SeO}_3\text{H}_2^+$	0.9194	2293
3	»Fe-OH-SeO_3^{2-}, $\text{»Fe-OH}_2\text{-HSeO}_3$, $(\text{»Fe-OH}_2)_2\text{-SeO}_3$	0.9234	2250
3	»Fe-OH-SeO_3^{2-}, $\text{»Fe-OH}_2\text{-SeO}_3\text{H}_2^+$, $(\text{»Fe-OH}_2)_2\text{-SeO}_3$	0.9217	2245

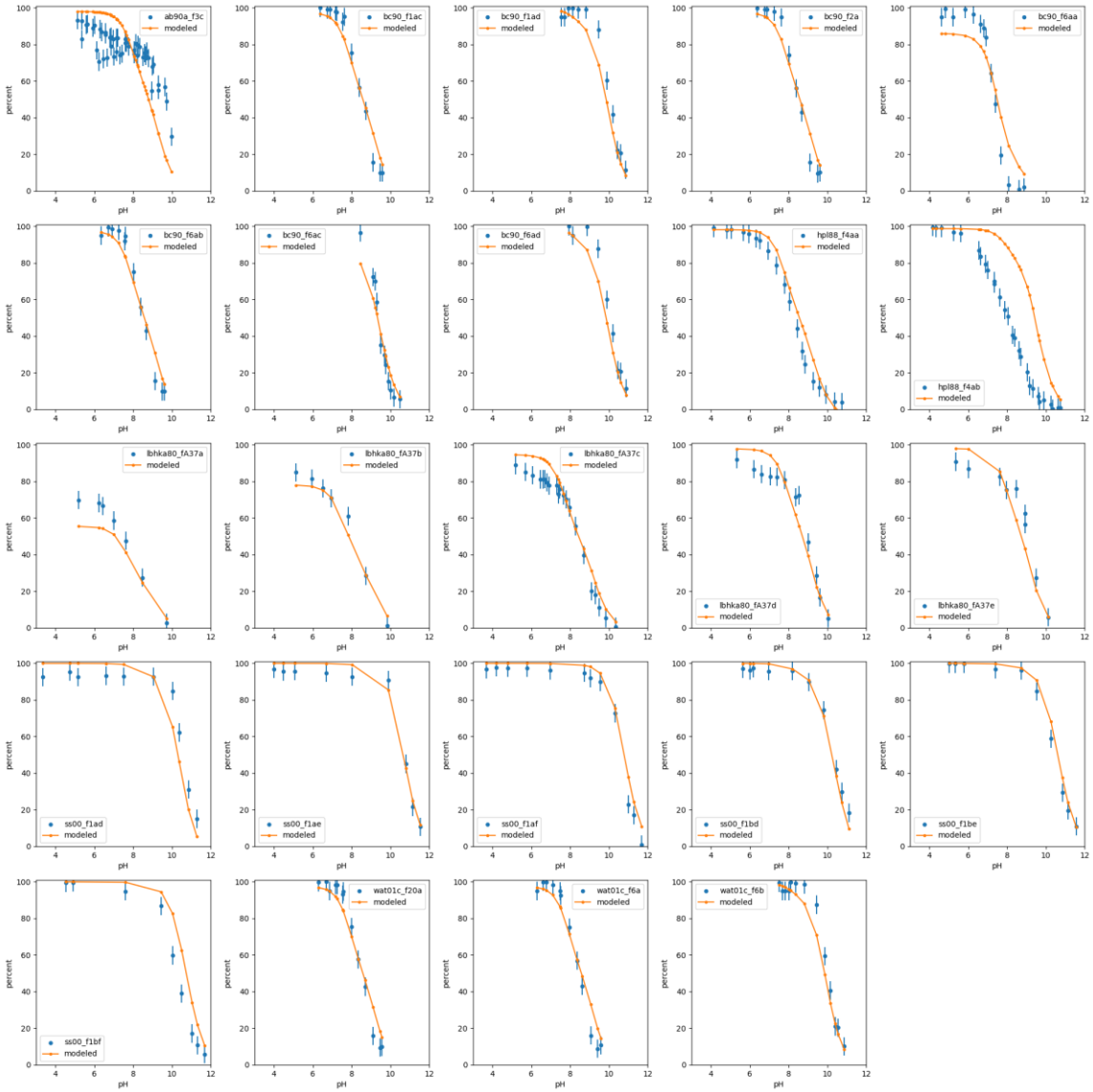

Figure 12. Simulation results for Se(IV) sorption to ferrihydrite. The results obtained from scenario 22 in Table 5. Datapoints colored in blue represent experimental data and orange solid lines represent modeled data from L-ASCM.

4.3 Limitations of the modeling and further works

The model developed through the present task showed its ability for automation of simulation workflow for modeling sorption phenomena. Therefore, it was made possible to examine a lot of SCM constructs for obtaining the best quality model which can reproduce experimental data. However, several workflow processes remain to be improved. In SCM, both surface acidity constants and surface site density (SSD) of adsorbent, which are inherent characteristics of adsorbent, are essential input parameters. In spite of their importance, SCMs reported by various works often employed different values for those parameters. For this reason, community data driven surface titration modeling tool, L-ASTM (Figure 10), is under development. The model will enable more robust surface complexation modeling by providing ‘global’ surface acidity constants of

given minerals to L-ASCM. In addition, the SSDs calculated via a crystallographic approach will be used to avoid ambiguity in the selection of those values (Eibl et al., 2019; Neumann et al., 2021).

5. FY23 Efforts

Our FY23 effort focused on completing our analysis of radionuclide incorporation into Fe oxide phases and evaluation of λ_{Me} values across a range of radionuclides relevant to performance assessment models and demonstrating our approach using Se as an example. Based on our assessment of the relevance of this process in radionuclide retention and sequestration in corrosion products, we will complete our analysis for a number of relevant radionuclides and plan to initiate focused corrosion and coprecipitation experiments to that will address the limitations of data available in the literature. For example, no data are available for the incorporation of I into corrosion products. As a result, we are not able to assess its potential impact on I migration from repository near fields. The scope of experiments will be determined in consultation with SFWST and the needs of the program and GDSA. Additionally, although there is a significant body of literature discussing sorption processes of Se species with various reduced Fe minerals (Fe(II) and mixed Fe(II/FeIII)), there is a lack of information regarding the fate of Se species during re-oxidation. Future studies should focus on determining the retention mechanisms of Se species after extended disposure to oxidative conditions, as has been done for Tc.

Our analysis of Se sorption to iron oxide phases will be enhanced by explicitly accounting for surface titration information and reactive site density parameters in our surface complexation modeling workflow. This analysis will yield a more robust workflow for developing self-consistent surface complexation modeling approaches that can be adapted to specific SCM conceptual and numerical approaches (i.e. non-electrostatic, diffuse layer, triple layer models). The workflow will then be extended to a more comprehensive survey of radionuclides and mineral surfaces relevant to the nuclear waste repository performance assessment modeling effort.

6. Acknowledgments

This work was supported by the Spent Fuel and Waste Science and Technology campaign of the Department of Energy's Nuclear Energy Program. Prepared by LLNL under Contract DE-AC52-07NA27344.

7. References

Abraitis P. K., Pattrick R. A. D. and Vaughan D. J. (2004) Variations in the compositional, textural and electrical properties of natural pyrite: a review. *Int J Miner Process* **74**, 41-59.

Adegoke H. I., Adekola F. A., Fatoki O. S. and Ximba B. J. (2013) Sorptive Interaction of Oxyanions with Iron Oxides: A Review. *Pol J Environ Stud* **22**, 7-24.

Anderson P. R. and Benjamin M. M. (1990) Surface and Bulk Characteristics of Binary Oxide Suspensions. *Environ Sci Technol* **24**, 692-698.

Balboni E., Smith K. F., Moreau L. M., Wimpenny J., Booth C. H., Kersting A. B. and Zavarin M. (2021) Plutonium Co-precipitation with Calcite. *ACS Earth and Space Chemistry* **5**, 3362-3374.

Balboni E., Smith K. F., Moreau L. M., Li T. T., Maloubier M., Booth C. H., Kersting A. B. and Zavarin M. (2020) Transformation of Ferrihydrite to Goethite and the Fate of Plutonium. *ACS Earth and Space Chemistry* **4**, 1993-2006.

Balistrieri L. S. and Chao T. T. (1987) Selenium Adsorption by Goethite. *Soil Sci Soc Am J* **51**, 1145-1151.

Balistrieri L. S. and Chao T. T. (1990a) Adsorption of selenium by amorphous iron oxyhydroxide and manganese dioxide. *Geochim Cosmochim Ac* **54**, 739-751.

Balistrieri L. S. and Chao T. T. (1990b) Adsorption of Selenium by Amorphous Iron Oxyhydroxide and Manganese-Dioxide. *Geochim Cosmochim Ac* **54**, 739-751.

Barescut J. C., Gariel J. C., Péres J. M., Février L. and Martin-Garin A. (2005) Biogeochemical behaviour of anionic radionuclides in soil: Evidence for biotic interactions. *Radioprotection* **40**, S79-S86.

Benjamin M. M. and Bloom N. S. (1981) Effects of Strong Binding of Anionic Adsorbates on Adsorption of Trace Metals on Amorphous Iron Oxyhydroxide. In *Adsorption From Aqueous Solutions* (ed. P. H. Tewari). Springer US, Boston, MA. pp. 41-60.

Bildstein O., Trotignon L., Perronnet M. and Jullien M. (2006) Modelling iron-clay interactions in deep geological disposal conditions. *Phys Chem Earth* **31**, 618-625.

Bingham P. A., Connelly A. J., Cassingham N. J. and Hyatt N. C. (2011) Oxidation state and local environment of selenium in alkali borosilicate glasses for radioactive waste immobilisation. *J Non-Cryst Solids* **357**, 2726-2734.

Bolanz R. M., Wierzbicka-Wieczorek M., Caplovicova M., Uhlik P., Gottlicher J., Steininger R. and Majzlan J. (2013) Structural Incorporation of As5+ into Hematite. *Environ Sci Technol* **47**, 9140-9147.

Borsig N., Scheinost A. C., Shaw S., Schild D. and Neumann T. (2018) Retention and multiphase transformation of selenium oxyanions during the formation of magnetite via iron(II) hydroxide and green rust. *Dalton Transactions* **47**, 11002-11015.

Börsig N., Scheinost A. C., Shaw S., Schild D. and Neumann T. (2017) Uptake mechanisms of selenium oxyanions during the ferrihydrite-hematite recrystallization. *Geochim Cosmochim Ac* **206**, 236-253.

Boult K. A., Cowper M. M., Heath T. G., Sato H., Shibutani T. and Yui M. (1998) Towards an understanding of the sorption of U(VI) and Se(IV) on sodium bentonite. *Journal of Contaminant Hydrology* **35**, 141-150.

Brendler V., Vahle A., Arnold T., Bernhard G. and Fanghänel T. (2003) RES3T-Rossendorf expert system for surface and sorption thermodynamics. *J Contam Hydrol* **61**, 281-291.

Chen F. R., Burns P. C. and Ewing R. C. (1999) Se-79: geochemical and crystallo-chemical retardation mechanisms. *Journal of Nuclear Materials* **275**, 81-94.

Curti E. (1999) Coprecipitation of radionuclides with calcite: estimation of partition coefficients based on a review of laboratory investigations and geochemical data. *Applied Geochemistry* **14**, 433-445.

Curti E., Puranen A., Grolimund D., Jädernas D., Sheptyakov D. and Mesbah A. (2015) Characterization of selenium in UO2 spent nuclear fuel by micro X-ray absorption spectroscopy and its thermodynamic stability. *Environmental Science: Processes & Impacts* **17**, 1760-1768.

Curti E., Froideval-Zumbiehl A., Günther-Leopold I., Martin M., Bullemer A., Linder H., Borca C. N. and Grolimund D. (2014) Selenium redox speciation and coordination in high-burnup UO2 fuel: Consequences for the release of 79Se in a deep underground repository. *Journal of Nuclear Materials* **453**, 98-106.

Das S., Essilfie-Dughan J. and Hendry M. J. (2015) Fate of adsorbed arsenate during phase transformation of ferrihydrite in the presence of gypsum and alkaline conditions. *Chemical Geology* **411**, 69-80.

Davis J. A. and Leckie J. O. (1980) Surface ionization and complexation at the oxide/water interface. 3. Adsorption of anions. *J Colloid Interf Sci* **74**, 32-43.

De Craen M., Van Geet M., Wang L. and Put M. (2004) High sulphate concentrations in squeezed Boom Clay pore water: evidence of oxidation of clay cores. *Phys Chem Earth* **29**, 91-103.

Diener A. and Neumann T. (2011) Synthesis and incorporation of selenide in pyrite and mackinawite. *Radiochim Acta* **99**, 791-798.

Diener A., Neumann T., Kramar U. and Schild D. (2012) Structure of selenium incorporated in pyrite and mackinawite as determined by XAFS analyses. *Journal of Contaminant Hydrology* **133**, 30-39.

Doerner H. A. and Hoskins W. M. (1925) Co-precipitation of radium and barium sulfates. *Journal of the American Chemical Society* **47**, 662-675.

Doherty J. (2018) PEST: Model-Independent Parameter Estimation. Watermark Numerical Computing.

Dresden-Rossendorf H.-Z. (2013) RES³T - Rossendorf Expert System for Surface and Sorption Thermodynamics. https://www.hzdr.de/db/RES3T.disclaimer.

Duc M., Lefèvre G. and Fédoroff M. (2006) Sorption of selenite ions on hematite. *J Colloid Interf Sci* **298**, 556-563.

Duc M., Lefevre G., Fedoroff M., Jeanjean J., Rouchaud J. C., Monteil-Rivera F., Dumonceau J. and Milonjic S. (2003) Sorption of selenium anionic species on apatites and iron oxides from aqueous solutions. *J Environ Radioactiv* **70**, 61-72.

Dzombak D. A. and Morel F. M. M. (1990) *Surface complexation modeling: hydrous ferric oxide*. John Wiley & Sons.

Eibl M., Virtanen S., Pischel F., Bok F., Lönnrot S., Shaw S. and Huittinen N. (2019) A spectroscopic study of trivalent cation (Cm^{3+} and Eu^{3+}) sorption on monoclinic zirconia (ZrO_2). *Applied Surface Science* **487**, 1316-1328.

Fernández-Martínez A. and Charlet L. (2009) Selenium environmental cycling and bioavailability: a structural chemist point of view. *Reviews in Environmental Science and Bio/Technology* **8**, 81-110.

Fevrier L., Martin-Garin A. and Leclerc E. (2007) Variation of the distribution coefficient (K-d) of selenium in soils under various microbial states. *J Environ Radioactiv* **97**, 189-205.

Francisco P. C. M., Sato T., Otake T., Kasama T., Suzuki S., Shiwaku H. and Yaita T. (2018) Mechanisms of Se(IV) Co-precipitation with Ferrihydrite at Acidic and Alkaline Conditions and Its Behavior during Aging. *Environ Sci Technol* **52**, 4817-4826.

Galvez N., Barron V. and Torrent J. (1999) Effect of phosphate on the crystallization of hematite, goethite, and lepidocrocite from ferrihydrite. *Clay Clay Miner* **47**, 304-311.

Gaucher E., Robelin C., Matray J. M., Negral G., Gros Y., Heitz J. F., Vinsot A., Rebours H., Cassagnabere A. and Bouchet A. (2004) ANDRA underground research laboratory: interpretation of the mineralogical and geochemical data acquired in the Callovian-Oxfordian formation by investigative drilling. *Phys Chem Earth* **29**, 55-77.

Grambow B. (2008) Mobile fission and activation products in nuclear waste disposal. *Journal of Contaminant Hydrology* **102**, 180-186.

Hayes K. F., Papelis C. and Leckie J. O. (1988) Modeling ionic strength effects on anion adsorption at hydrous oxide/solution interfaces. *J Colloid Interf Sci* **125**, 717-726.

Hayes K. F., Roe A. L., Brown Jr G. E., Hodgson K. O., Leckie J. O. and Parks G. A. (1987) In situ x-ray absorption study of surface complexes: Selenium oxyanions on α-FeOOH. *Science* **238**, 783-786.

Hayes Kim F., Roe A. L., Brown Gordon E., Hodgson Keith O., Leckie James O. and Parks George A. (1987) In Situ X-ray Absorption Study of Surface Complexes: Selenium Oxyanions on α-FeOOH. *Science* **238**, 783-786.

Hingston F. J., Posner A. M. and Quirk J. P. (1971) Competitive adsorption of negatively charged ligands on oxide surfaces. *Discussions of the Faraday Society* **52**, 334-342.

Iida Y., Tanaka T., Yamaguchi T. and Nakayama S. (2011) Sorption Behavior of Selenium(-II) on Rocks under Reducing Conditions. *J Nucl Sci Technol* **48**, 279-291.

Jordan N., Lomenech C., Marmier N., Giffaut E. and Ehrhardt J.-J. (2009) Sorption of selenium(IV) onto magnetite in the presence of silicic acid. *J Colloid Interf Sci* **329**, 17-23.

Jordan N., Ritter A., Scheinost A. C., Weiss S., Schild D. and Hübner R. (2014a) Selenium(IV) Uptake by Maghemite (γ-Fe2O3). *Environ Sci Technol* **48**, 1665-1674.

Jordan N., Ritter A., Scheinost A. C., Weiss S., Schild D. and Hubner R. (2014b) Selenium(IV) Uptake by Maghemite (gamma-Fe2O3). *Environ Sci Technol* **48**, 1665-1674.

Jordan N., Ritter A., Foerstendorf H., Scheinost A. C., Weiss S., Heim K., Grenzer J., Mucklich A. and Reuther H. (2013) Adsorption mechanism of selenium(VI) onto maghemite. *Geochim Cosmochim Ac* **103**, 63-75.

Jörg G., Bühnemann R., Hollas S., Kivel N., Kossert K., Van Winckel S. and Gostomski C. L. v. (2010) Preparation of radiochemically pure 79Se and highly precise determination of its half-life. *Applied Radiation and Isotopes* **68**, 2339-2351.

Joseph C., Schmeide K., Sachs S., Brendler V., Geipel G. and Bernhard G. (2011) Sorption of uranium(VI) onto Opalinus Clay in the absence and presence of humic acid in Opalinus Clay pore water. *Chemical Geology* **284**, 240-250.

Kim S. S., Min J. H., Lee J. K., Baik M. H., Choi J.-W. and Shin H. S. (2012) Effects of pH and anions on the sorption of selenium ions onto magnetite. *J Environ Radioactiv* **104**, 1-6.

Kingston F. J., Posner A. M. and Quirk J. P. (1972) ANION ADSORPTION BY GOETHITE AND GIBBSITE. *Journal of Soil Science* **23**, 177-192.

Leckie J. O., Benjamin M. M., Hayes K., Kaufman G. and Altmann S. (1980) Adsorption/coprecipitation of trace elements from water with iron oxyhydroxide. Electric Power Research Institute, Palo Alto, CA, USA

Liu J., Liang C., Zhang H., Tian Z. and Zhang S. (2012) General Strategy for Doping Impurities (Ge, Si, Mn, Sn, Ti) in Hematite Nanocrystals. *The Journal of Physical Chemistry C* **116**, 4986-4992.

López de Arroyabe Loyo R., Nikitenko S. I., Scheinost A. C. and Simonoff M. (2008) Immobilization of Selenite on Fe3O4 and Fe/Fe3C Ultrasmall Particles. *Environ Sci Technol* **42**, 2451-2456.

Martínez M., Giménez J., de Pablo J., Rovira M. and Duro L. (2006) Sorption of selenium(IV) and selenium(VI) onto magnetite. *Applied Surface Science* **252**, 3767-3773.

Missana T., Alonso U. and Garcia-Gutierrez M. (2009a) Experimental study and modelling of selenite sorption onto illite and smectite clays. *J Colloid Interf Sci* **334**, 132-138.

Missana T., Alonso U., Scheinost A. C., Granizo N. and García-Gutiérrez M. (2009b) Selenite retention by nanocrystalline magnetite: Role of adsorption, reduction and dissolution/co-precipitation processes. *Geochim Cosmochim Ac* **73**, 6205-6217.

Morse J. W. (1994) Interactions of Trace-Metals with Authigenic Sulfide Minerals - Implications for Their Bioavailability. *Mar Chem* **46**, 1-6.

Morse J. W. and Luther G. W. (1999) Chemical influences on trace metal-sulfide interactions in anoxic sediments. *Geochim Cosmochim Ac* **63**, 3373-3378.

Neumann J., Brinkmann H., Britz S., Lützenkirchen J., Bok F., Stockmann M., Brendler V., Stumpf T. and Schmidt M. (2021) A comprehensive study of the sorption mechanism and thermodynamics of f-element sorption onto K-feldspar. *J Colloid Interf Sci* **591**, 490-499.

Nie Z., Finck N., Heberling F., Pruessmann T., Liu C. and Lützenkirchen J. (2017) Adsorption of Selenium and Strontium on Goethite: EXAFS Study and Surface Complexation Modeling of the Ternary Systems. *Environ Sci Technol* **51**, 3751-3758.

Nothstein A. K., Eiche E., Riemann M., Nick P., Winkel L. H. E., Gottlicher J., Steininger R., Brendel R., von Brasch M., Konrad G. and Neumann T. (2016) Tracking Se Assimilation and Speciation through the Rice Plant - Nutrient Competition, Toxicity and Distribution. *Plos One* **11**.

Olyslaegers G., Zeevaert T., Pinedo P., Simon I., Prohl G., Kowe R., Chen Q., Mobbs S., Bergstrom U., Hallberg B., Katona T., Eged K. and Kanyar B. (2005) A comparative radiological assessment of five European biosphere systems in the context of potential contamination of well water from the hypothetical disposal of radioactive waste. *J Radiol Prot* **25**, 375-391.

Parkhurst D. L. and Appelo C. A. J. (2013) Description of input and examples for PHREEQC version 3—A computer program for speciation, batch-reaction, one-dimensional transport, and inverse geochemical calculations, US geological survey techniques and methods, p. 497.

Rickard D. and Luther G. W. (2007) Chemistry of iron sulfides. *Chem Rev* **107**, 514-562.

Rietra R. P. J. J., Hiemstra T. and van Riemsdijk W. H. (2001) Comparison of selenate and sulfate adsorption on goethite. *J Colloid Interf Sci* **240**, 384-390.

Roh Y., Lee S. Y. and Elless M. P. (2000) Characterization of corrosion products in the permeable reactive barriers. *Environ Geol* **40**, 184-194.

Rovira M., Giménez J., Martínez M., Martínez-Lladó X., de Pablo J., Martí V. and Duro L. (2008) Sorption of selenium(IV) and selenium(VI) onto natural iron oxides: Goethite and hematite. *Journal of Hazardous Materials* **150**, 279-284.

Schwertmann U. and Cornell R. M. (2000) Iron oxides in the laboratory. In *Iron Oxides in the Laboratory*. Wiley-VCH Verlag GmbH. pp. i-xviii.

Séby F., Potin-Gautier M., Giffaut E., Borge G. and Donard O. F. X. (2001) A critical review of thermodynamic data for selenium species at 25°C. *Chemical Geology* **171**, 173-194.

Skomurski F. N., Rosso K. M., Krupka K. M. and McGrail B. P. (2010) Technetium Incorporation into Hematite (alpha-Fe2O3). *Environ Sci Technol* **44**, 5855-5861.

Su C. M. and Suarez D. L. (2000) Selenate and selenite sorption on iron oxides: An infrared and electrophoretic study. *Soil Sci Soc Am J* **64**, 101-111.

Wang P., Anderko A. and Turner D. R. (2001a) Thermodynamic modeling of the adsorption of radionuclides on selected minerals. II: Anions. *Ind Eng Chem Res* **40**, 4444-4455.

Wang P. M., Anderko A. and Turner D. R. (2001b) Thermodynamic modeling of the adsorption of radionuclides on selected minerals. I: Cations. *Industrial & Engineering Chemistry Research* **40**, 4428-4443.

Winkel L. H. E., Vriens B., Jones G. D., Schneider L. S., Pilon-Smits E. and Banuelos G. S. (2015) Selenium Cycling Across Soil-Plant-Atmosphere Interfaces: A Critical Review. *Nutrients* **7**, 4199-4239.

Zavarin M., Chang E., Wainwright H., Parham N., Kaukuntla R., Zouabe J., Deinhart A., Genetti V., Shipman S., Bok F. and Brendler V. (2022) Community Data Mining Approach for Surface Complexation Database Development. *Environ Sci Technol* **56**, 2827-2838.

Zhang P. and Sparks D. L. (1990) Kinetics of selenate and selenite adsorption/desorption at the goethite/water interface. *Environ Sci Technol* **24**, 1848-1856.